

Article

# Control of a Fault-Tolerant Photovoltaic Energy Converter in Island Operation

Marino Coppola <sup>1,\*</sup>, Pierluigi Guerriero <sup>1</sup>, Adolfo Dannier <sup>1</sup>, Santolo Daliento <sup>1</sup>,  
Davide Lauria <sup>2</sup> and Andrea Del Pizzo <sup>1</sup>

<sup>1</sup> Department of Electrical Engineering and Information Technologies, University of Napoli Federico II, Via Claudio 21, 80125 Napoli, Italy; pierluigi.guerriero@unina.it (P.G.); adannier@unina.it (A.D.); daliento@unina.it (S.D.); delpizzo@unina.it (A.D.P.)

<sup>2</sup> Department of Industrial Engineering, University of Napoli Federico II, Via Claudio 21, 80125 Napoli, Italy; dlauria@unina.it

\* Correspondence: marino.coppola@unina.it; Tel.: +39-081-7683228

Received: 14 May 2020; Accepted: 17 June 2020; Published: 19 June 2020



**Abstract:** The paper deals with design and control of a fault tolerant and reconfigurable photovoltaic converter integrating a Battery Energy Storage System as a standby backup energy resource. When a failure occurs, an appropriate control method makes the energy conversion system capable of operating in open-delta configuration in parallel with the grid as well as in islanded mode. In case network voltage is lacking due to heavy anomalies or maintenance reasons, the proposed control system is able to quickly disconnect the inverter from the grid while ensuring the energy continuity to the local load and the emergency fixtures by means of the integrated battery packs. In particular, the paper proposes a fast islanding detection method essential for the correct operation of the control system. This specific technique is based on the Hilbert transform of the voltage of the point of common coupling, and it identifies the utility lack in a period of time equal to half a grid cycle in the best case (i.e., 10 ms), thus resulting in good speed performance fully meeting the standard requirements. A thorough numerical investigation is carried out with reference to a representative case study in order to demonstrate the feasibility and the effectiveness of the proposed control strategy.

**Keywords:** power systems for renewable energy; fault-tolerant photovoltaic inverter; islanding detection; energy storage system

## 1. Introduction

Over the last years, the electric energy generated from renewable energy sources (RES) has grown exponentially. In particular, photovoltaic (PV) energy has now become one of the most relevant parts in energy mix in several geographical areas [1]. In such a scenario, as most of the installed PV generators (PVGs) are grid connected, particular attention must be paid to the system reliability [2] in order to meet the requirements of the electric service in terms of efficiency and power quality. Moreover, the continuous increase in capacity of the PV installed plants makes these resources an important agent in active distribution grids, as they are distributed energy resources (DER) also requiring special control strategies [3]. As a consequence, one of the main purposes of the research is to facilitate the integration of variable renewable sources and distributed generation units within the grid [4].

A particular condition arises when a PV DER feeds a critical local load or emergency fixtures in a grid-tied system; it should be capable of operating in parallel with the grid as well as in island (i.e., regardless of the mains). In fact, the island operating mode becomes unavoidable in case of power outage (e.g., for fault conditions or maintenance purposes) in order to ensure continuous energy supply to the local loads. Obviously, in islanded mode, the inherent intermittent nature of PV generation does

not allow fulfillment of the load power demand. For this reason, the integration of a Battery Energy Storage System (BESS) as a standby backup energy resource can be useful to guarantee continuity of the power supply or at least to compensate for the gap between load demand and PV production. Thus, a proper control action must be implemented to ensure the capability of the overall system to work in different operating modes [5]. The islanding detection (ID) and the consequent disconnection from the grid are significant features that the system must implement. In technical literature, different detection techniques are analyzed [6–11]. The ID methods (IDMs) are mainly divided into two categories: local and remote methods. Local IDMs are then classified as passive and active methods. The former methods are based on the monitoring of change or the rate of change in the power system parameters, while the latter rely on the injection of a small perturbation in the output system parameters to identify islanding condition. Comprehensive review and performance evaluations of the several proposed techniques are reported in [10,11]. One of the most relevant figures of merit (FoM) to compare the various IDMs is the time requested to identify the grid trip (i.e., detection time or speed), which should be lower than the standard requirements. In [10,11], active, passive, and modified passive methods based on signal processing are compared in terms of speed. In particular, among the passive methods, the wavelet transform (WT) technique seems to reach the best speed performance but at the cost of increased computational complexity. Recent research works [12–17] propose enhanced IDMs; [12] reports a feedback-based passive islanding detection technique for one-cycle-controlled (OCC) single-phase inverter used in photovoltaic system. This method, as stated by the authors, is not generic and limited to OCC-based inverters while providing a detection time of about 200 ms (i.e., 10 grid cycles). In [13], an IDM based on parallel inductive impedance (PII) switching at a distributed generation (DG) connection point along with monitoring the rate of change of voltage at the DG output is implemented. However, to identify the islanding, this technique needs a two-step procedure that requires at least 300 ms in the worst case, corresponding to a run-on time of 15 grid cycles. In [14], a methodology to detect islanding in a grid-connected photovoltaic system is proposed. A disturbance is injected into the maximum power point tracking (MPPT) algorithm when the absolute deviation of the point of common coupling (PCC) voltage in any phase exceeds a voltage threshold. This determines a shift of the system operating point from its maximum power point (MPP), thus resulting in a relevant output power reduction, and the detection time results within 300 ms (i.e., 15 grid cycles). In [15], the used method for adjustment and evaluation of a voltage relay is based on the combination of the application region (AR) and the power imbalance application region (PIAR) methods, and it leads to a detection time of hundreds of milliseconds (i.e., 100–400 ms, 5–20 grid cycles). In [16], a combination of rate of change of frequency (ROCOF), rate of change of phase angle difference (ROCPAD), rate of change of voltage (ROCOV), and over frequency/under frequency (OF/UF) methods is reported. In such a case, the proposed algorithm represents the merge of different passive ID techniques, thus the detection time is always the minimum among the different used algorithms. As a consequence, it seems to work well (e.g., detection time of few milliseconds) but at the cost of a more complex implementation. A variance in the autocorrelation of the modal current envelope (VAMCE) is used as an islanding detection criterion in [17]. This method employs an autocorrelation function (ACF) of a modal current envelope derived by Hilbert transform, and its detection time is of about two or three grid cycles (i.e., 40–60 ms).

This paper proposes a kind of passive method based on the observation of the envelope of the voltage of the point of common coupling. The envelope of the considered quantity is quickly obtained by means of the Hilbert transform and specifically the proposed algorithm outputs the absolute value of the Hilbert transform that can represent a reliable index of fast change in network behavior. In fact, the grid trip phenomenon causes a sudden variation of the PCC voltage, which results in a spike of the monitored quantity. The latter may no longer fall within a predefined safety range, thus allowing islanding detection according to the requirements of the network code. In principle, the monitoring of the envelope does not need to wait for the PCC voltage crest to verify the boundaries' violation, thus leading to a detection time less than a grid cycle (i.e., 10 ms in the best case), thus showing its benefit in

terms of speed with respect to the aforementioned techniques. In addition, the proposed method can be used independently of the specific application.

The paper describes a control strategy that is used to implement grid-connected and intentional islanding operations of a PV inverter when the power circuits are in open-delta configuration as a consequence of a local fault. Under ordinary operating conditions, the PV source delivers the energy to the load and, if the load request is not met, the grid provides the residual part while the battery is in idle mode. In islanded mode, the continuous power supply of the load is ensured due to the integrated BESS, thus overcoming the lack of grid supply and obtaining a flat profile of the inverter output power [18].

The starting architecture for the considered energy conversion system is the conventional double-stage configuration of Figure 1. It represents a centralized solution in which PVG is made up of several strings in parallel in order to achieve the desired rated power.

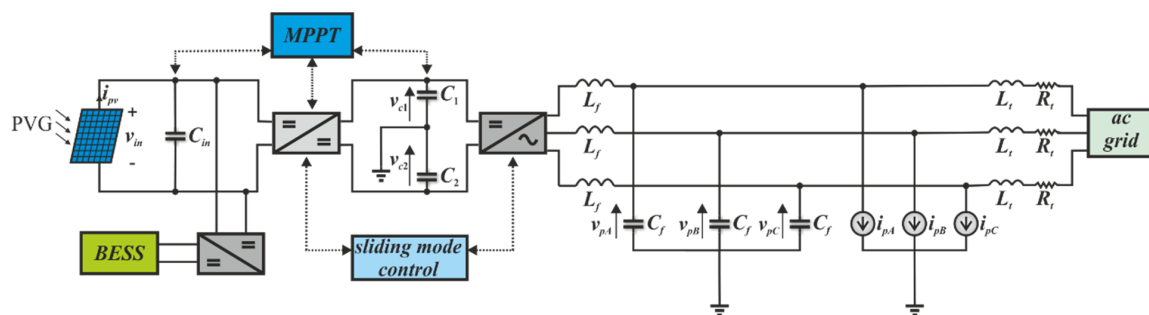


**Figure 1.** Schematic view of double-stage three-phase photovoltaic (PV) inverter with integrated Battery Energy Storage System (BESS).

In a previous paper [19], the authors proposed a solution to enhance fault tolerance of the system and its reliability, introducing a particular control strategy aimed at operating even with only two legs (phases) still being fully functional. In fact, in case of failure of one inverter leg, dedicated switches are capable of short-circuiting the LC filter ( $L_f - C_f$ ) of the failing leg, leading to the new open-delta configuration shown in Figure 2, which allows the PV inverter to operate even in the presence of a fault. With reference to the two-leg configuration of the inverter, the effect of BESS integration and the effectiveness of the proposed ID method are discussed.

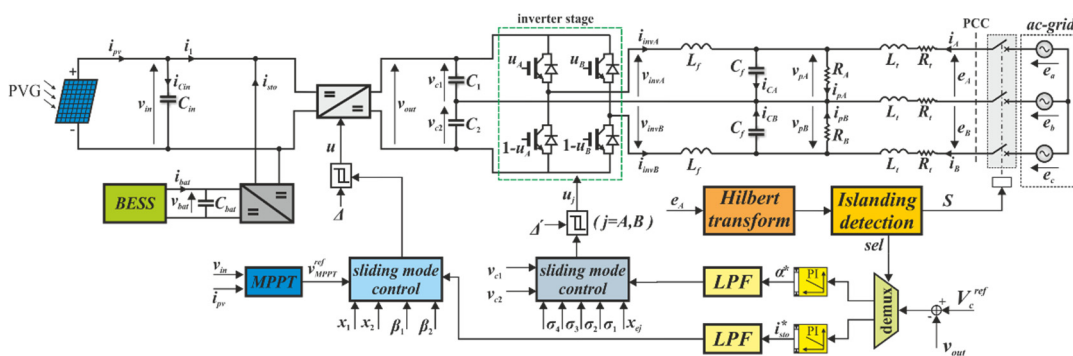


**Figure 2.** Overall system configuration.

The paper is organized as follows. System modeling is reported in Section 2. Then, Section 3 deals with design and control of the grid-tied PV inverter. In Section 4, the proposed design procedure is validated by carrying out numerical simulations in PLECS environment. Conclusions are summarized in Section 5.

## 2. System Modeling

The power inverter in the “two legs” configuration shown in Figure 2 is arranged in a double-stage architecture. The first power stage is a step-up DC-DC converter with coupled inductors [20–22] that allows high efficiency and high voltage gain (see Figure 3). It consists of a primary inductor  $L_1$  and a secondary inductor  $L_2$ , while resistors  $R_1$  and  $R_2$  account for inductors copper losses.

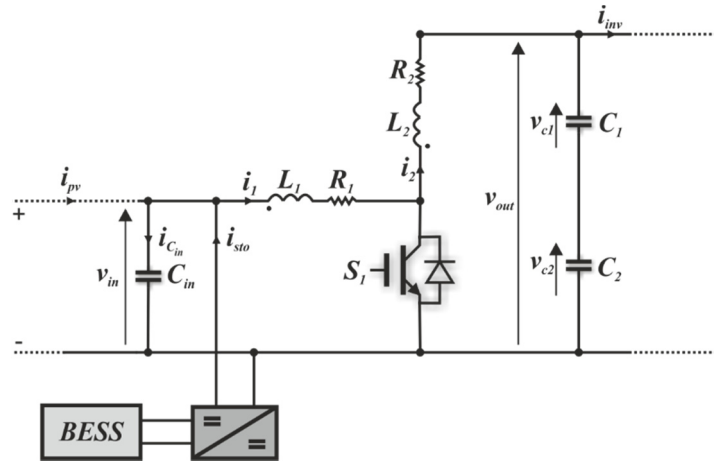


Figure 3. First power stage with coupled-inductors and BESS.

The winding ratio of the magnetically coupled inductors is equal to  $r_n = N_2/N_1$ , where  $N_1$  and  $N_2$  are the turn numbers of the primary and the secondary inductor, respectively. In our analysis, the coupling coefficient  $k$  is considered ideal (i.e.,  $k = 1$ ), thus the total inductance is  $L = (N_1 + N_2)^2 L_0$ , with  $L_0$  the inductance of a single winding. The integrated BESS is connected to the input DC-link through an auxiliary bidirectional DC-DC converter.

With reference to Figure 3, the mathematical model of the coupled inductors converter can be expressed as:

$$\begin{cases} \frac{d i_m}{d t} = \frac{v_{in}-R_1 i_m}{L_1} u + \frac{v_{in}-v_{out}}{L_1(1+r_n)}(1-u) - \frac{R_1+R_2}{L_1(1+r_n)^2} i_m(1-u) \\ \frac{d v_{in}}{d t} = \frac{i_{pv}+i_{sto}}{C_{in}} - \frac{i_m}{C_{in}} u - \frac{i_m}{(1+r_n)C_{in}}(1-u) \\ \frac{d v_{out}}{d t} = \frac{2 i_m}{(1+r_n)C} (1-u) - \frac{2 i_{inv}}{C} \end{cases} \quad (1)$$

where  $u \in \{0,1\}$ . More specifically,  $u = 1$  when  $S_1$  is ON;  $u = 0$  when  $S_1$  is OFF. Moreover,  $C$  is equal to  $C_1 = C_2$ .

The second power stage is a two-phase DC-AC inverter, where the phase  $A$  is supplied by the line-to-line voltage  $e_A$ , and the phase  $B$  by  $e_B$ , while the generated output inverter voltages are  $v_{invA}$  and  $v_{invB}$ . The two capacitors  $C_1 = C_2$  ensure the power decoupling with respect to the first power stage. The inverter supplies the local load modeled by means of two properly sized resistors (i.e.,  $R_A, R_B$ ) through a filter ( $L_f - C_f$ ). The load is clearly unbalanced, but, as demonstrated below, the inverter is always capable of carrying out an effective balancing action. At the network side, the line three-phase transformer is modeled by the equivalent parameters  $R_t - L_t$ , which also includes a suitable series inductance to decouple the inverter from the grid with the aim of reaching better performance in terms of power quality. Considering the circuit in Figure 2, the following Equations can be written:

$$\begin{cases} \frac{d i_j}{d t} = \frac{2}{3L_t} (e_j - 2 R_t i_j - v_{pj} - R_t i_k) - \frac{1}{3L_t} (e_k - 2 R_t i_k - v_{pk} - R_t i_j) \\ \frac{d i_{invj}}{d t} = \frac{1}{L_f} (v_{invj} - v_{pj}) \\ \frac{d v_{pj}}{d t} = \frac{1}{C_f} (i_j + i_{invj} - i_{pj}) \end{cases} \quad (2)$$

where the subscript indexes  $j, k \in \{A, B\}$  with  $j \neq k$ , while the dynamic behavior of DC-link voltages is given by:

$$\begin{cases} \frac{d v_{c1}}{d t} = -\frac{1}{C_1} (u_A i_{invA} + u_B i_{invB}) + \frac{i_m(1-u)}{C_1(1+r_n)} \\ \frac{d v_{c2}}{d t} = \frac{1}{C_2} [(1-u_A) i_{invA} + (1-u_B) i_{invB}] + \frac{i_m(1-u)}{C_2(1+r_n)} \end{cases} \quad (3)$$

It should be noted that only the two line-to-line voltages  $v_{pA}$  and  $v_{pB}$  are controlled in open-delta connection. At the ac network side, a circuit breaker can disconnect the inverter from the grid if this is tripped, thus forcing the operating mode changing from “normal operation” to “islanded mode” in order to meet the requirements of the new circuit configuration.

### 3. System Control

The controller design plays a very important role in order to guarantee safe and reliable interconnection and interoperability of DER with electric power systems (EPS) as requested by the standard rules [23]. Instead of traditional linear control methods, a sliding mode technique is adopted to control the power stages (i.e., DC-DC converter and inverter) with the aim of obtaining optimal performance in terms of fast dynamic response and robustness against uncertainties and disturbances. The sliding surface of the first power stage is developed to ensure a reduced ripple of the PV voltage, thus limiting fluctuations around the MPP. A suitable control of the inverter is implemented in order to keep balanced the voltages ( $v_{C1}$ ,  $v_{C2}$ ) at the inverter DC-link while ensuring higher power quality. In fact, in the two legs configuration (Figure 2), the midpoint at the DC-link capacitors ( $C_1 - C_2$ ) becomes a common-phase of the open-delta system. Consequently, the voltage unbalancing between the two capacitors is a relevant issue to be suitably controlled in order to prevent undesired effects.

The paper does not focus on the control of the power exchange between the BESS and the PV sources because of well-established control strategy, and the same applies for the battery management system (BMS). On the contrary, attention is paid to the possibility of enhancing the system reliability due to the BESS integration, thus ensuring fulfillment of the load power demand even if the grid is tripped. In fact, the BESS does not act during normal operation (i.e., grid connected operation) but only in island mode. In the latter case, the BESS can accumulate the excess of power from the PVG (i.e., charging mode) if the power required by the load is less than the generated one.

Otherwise, it can provide the power backup if the load requires more power than generated (i.e., discharging mode). This means that the presence of the storage unit allows a flat profile of the load power regardless of the inherent variability of PV power production. Therefore, BESS makes the system able to continuously feed the critical load, thus enhancing the overall reliability.

In normal operation, the control of the DC-AC stage must ensure the energy transfer to the grid with unitary power factor and sinusoidal network currents, also keeping the load and the DC voltages (i.e.,  $v_{C1}$ ,  $v_{C2}$ ) balanced. Thus, the dynamics of the DC-link voltage  $v_{out}$  are relevant to control the displacement angle  $\alpha$  (angle between load voltages and network voltages) during normal operation and the storage system during islanding.

As shown in Figure 2, the sliding controllers adapt to circuit configuration due to a de-multiplexer driven by a proper selection signal ( $sel$ ) derived from the islanding detection block, which also activates the circuit breaker by means of the signal  $S$ . In other words, the islanding detection block is able to autonomously change the operating mode from normal operation to islanded mode. The two different operating modes are described in the following sub-sections.

#### 3.1. Normal Operation

The normal operation is extensively reported in [19] and here partially recalled for sake of completeness and clarity. The sliding mode control approach features the variable structure nature of DC-DC converters; by means of a proper operation of the switches, the system is forced to reach a suitable selected surface (sliding surface) and to stay on it. As a consequence, the proper choice of the

state variables represents a challenge in order to define a state space averaged model of the converter. In particular, in our case, the state variables chosen are the magnetizing current  $i_m$ , as defined in [24], and the input voltage  $v_{in}$  in order to accomplish the need of MPP tracking by considering the intrinsic variability of PV power generation. The model in Equation (1) can be simplified by neglecting the  $i_{sto}$ . The vector  $\mathbf{x}$  of the state variables error is:

$$\mathbf{x} = [x_1, x_2]^T = [i_m - I_m^{ref}, v_{in} - V_{in}^{ref}]^T \quad (4)$$

Thus the following matrix format can be derived:

$$\dot{\mathbf{x}} = \mathbf{A} \mathbf{x} + \mathbf{B} u + \mathbf{A} \mathbf{z} + \mathbf{F} \quad (5)$$

$$\mathbf{A} = \begin{pmatrix} -\frac{R_1+R_2}{L_1(1+r_n)^2} & \frac{1}{L_1(1+r_n)} \\ -\frac{1}{(1+r_n)C_{in}} & 0 \end{pmatrix} \quad (6)$$

$$\mathbf{B} = \begin{pmatrix} \frac{v_{in}}{L_1} - \frac{R_1}{L_1} i_m - \frac{v_{in}-v_{out}}{L_1(1+r_n)} + \frac{R_1+R_2}{L_1(1+r_n)^2} i_m + \\ -\frac{i_m}{C_{in}} + \frac{i_m}{(1+r_n)C_{in}} \end{pmatrix} \quad (7)$$

$$\mathbf{F} = \begin{pmatrix} -\frac{v_{out}}{L_1(1+r_n)} \\ \frac{i_{pv}}{C_{in}} \end{pmatrix}; \quad \mathbf{z} = [I_m^{ref}, V_{out}^{ref}]^T \quad (8)$$

$$I_m^{ref} = \frac{1+r_n}{1-D} I_{out}^{ref} = \frac{1+r_n}{1-D} \frac{V_{in}^{ref}}{V_{out}^{ref}} i_{pv} \quad (9)$$

where the duty cycle reference value is estimated as:

$$D = \frac{1 - \frac{v_{in}}{v_{out}}}{1 + r_n \frac{v_{in}}{v_{out}}} \quad (10)$$

The chosen sliding surface is a linear combination of the state variables error:

$$S(\mathbf{x}) = \beta_1 x_1 + \beta_2 x_2 = \boldsymbol{\beta}^T \mathbf{x} \quad (11)$$

where  $\boldsymbol{\beta}^T = [\beta_1, \beta_2]$ . The proper choice of the latter coefficients determines the existence conditions of sliding mode [25]:

$$\begin{cases} \dot{S}(\mathbf{x}) < 0 & \text{if } S(\mathbf{x}) > 0 \\ \dot{S}(\mathbf{x}) > 0 & \text{if } S(\mathbf{x}) < 0 \end{cases} \quad (12)$$

The respect of the conditions of Equation (12) assures that all the system states near the sliding surface  $S(\mathbf{x}) = 0$  are directed towards it for both possible states of the converter switch [26].

With the aim of ensuring that the state of the system remains close to the sliding surface, a suitable operation is necessary for the switch, which links its state with the value of  $S(\mathbf{x})$ . The latter means that, in a practical case, a discontinuous control law must be defined by using a hysteresis band:

$$u = \begin{cases} 0 & \text{if } S(\mathbf{x}) > +\Delta \\ 1 & \text{if } S(\mathbf{x}) < -\Delta \end{cases} \quad (13)$$

where  $2\Delta$  is the amplitude of the hysteresis band in the sliding surface, being  $\Delta$  an arbitrary small positive quantity. The reference value ( $v_{MPPPT}^{ref}$ ) of the input voltage is provided by an MPPT algorithm based on a classical perturb and observe (P & O) technique. The voltage reference is sent to the sliding

mode controller, thus obtaining an adaptive sliding surface modified at each MPPT step to extract the maximum available power.

The control of the second power stage (i.e., inverter stage) is also based on the sliding approach.

During ordinary operation, the main control goal is to transfer the power generated by PV sources (and not drawn from the load) to the grid by properly adapting the displacement angle  $\alpha$  (angle between load voltages and network voltages) to the different operating conditions (i.e.,  $\alpha > 0$  means that the excess power is transferred to the grid, while  $\alpha < 0$  means that the grid provides the difference between load power demand and PV generation). The reference rms value of the line-to-line voltage on the load can be derived by assuming unity power factor at the grid side, thus obtaining:

$$V_p^{ref} = E \frac{\sin \beta}{\sin(\beta - \alpha)} \quad (14)$$

where  $\beta = \tan^{-1}(X_t/R_t)$ ,  $X_t = \omega L_t$ ,  $\omega$  is the grid angular frequency, and  $E$  is the value of both  $e_A$  and  $e_B$ .

The reference quantities (subscript index 2) for the load line-to-line voltages (i.e.,  $v_{pA}$ ,  $v_{pB}$ ) and for their derivative (subscript index 1) of the two-phase system are described by the vector:

$$\mathbf{x}_{rj} = [x_{rj1}, x_{rj2}]^T \quad (15)$$

and the two components of  $\mathbf{x}_{rj}$  for  $j = A, B$  are:

$$\begin{cases} x_{rA1} = -\sqrt{2} \omega V_p^{ref} \sin(\omega t + \vartheta + \alpha^*) \\ x_{rA2} = \sqrt{2} V_p^{ref} \cos(\omega t + \vartheta + \alpha^*) \\ x_{rB1} = -\sqrt{2} \omega V_p^{ref} \sin(\omega t + \vartheta + \alpha^* + \pi/3) \\ x_{rB2} = \sqrt{2} V_p^{ref} \cos(\omega t + \vartheta + \alpha^* + \pi/3) \end{cases} \quad (16)$$

where  $\vartheta$  is the phase angle of the grid voltage (at  $t = 0$ ). From Equations (15) and (16), the sinusoidal model of the inverter voltages can be reported in matrix form:

$$\dot{\mathbf{x}}_{rj} = \mathbf{A}_r \mathbf{x}_{rj} \quad j = A, B \quad (17)$$

with:

$$\mathbf{A}_r = \begin{pmatrix} 0 & -\omega^2 \\ 1 & 0 \end{pmatrix} \quad (18)$$

The vector of the state variables is:

$$\mathbf{x}_j = [x_{j1}, x_{j2}]^T = [\dot{v}_{pj}, v_{pj}]^T \quad j = A, B \quad (19)$$

then, the vector  $\mathbf{x}_{ej}$  of the state variables error can be derived as follows:

$$\mathbf{x}_{ej} = \mathbf{x}_{rj} - \mathbf{x}_j = [x_{rj1} - x_{j1}, x_{rj2} - x_{j2}]^T \quad j = A, B \quad (20)$$

The chosen inverter sliding surface (Equation (20)) is a function of the state variable error  $\mathbf{x}_{ej}$ , but also of the error of the average and the instantaneous values of the inverter input DC-link voltages in order to meet the requirements for a reliable control action able to avoid DC-link voltages imbalance that could appear for asymmetrical condition during charging transients.

$$S_j(\mathbf{x}_{ej}, v_{c1}, v_{c2}) = \sigma_1(x_{rj1} - x_{j1}) + \sigma_2(x_{rj2} - x_{j2}) + \sigma_3(\bar{v}_{c1} - \bar{v}_{c2}) + \sigma_4(v_{c1} - v_{c2}) \quad j = A, B \quad (21)$$

Moreover, this surface requires a proper hysteresis band, hence the control law becomes:

$$u_j = \begin{cases} 0 & \text{if } S_j(\mathbf{x}_{ej}, v_{c1}, v_{c2}) > +\Delta' \\ 1 & \text{if } S_j(\mathbf{x}_{ej}, v_{c1}, v_{c2}) < -\Delta' \end{cases} \quad j \in \{A, B\} \quad (22)$$

The choice of the hysteresis band  $\Delta'$  depends on the maximum switching frequency and on the filter design.

### 3.2. Islanding Detection

The continuity of power supply to critical local load should be guaranteed also in case of lack of utility grid supply (e.g., fault condition or maintenance purpose). For this purpose, the grid trip must be properly detected to quickly counteract to this event. Several IDMs have been proposed. They can be classified in two main categories: passive and active methods. The former methods are based on the detection of a change or the rate of change in a power system parameter, while the latter are generally based on the introduction of small perturbations at the inverter output, thus generating small changes in a parameter of the power system [6]. As already discussed in the introduction, the proposed method is based on the pure observation of the envelope of the PCC voltage (e.g.,  $e_A$  in Figure 2) obtained by performing the absolute value of the Hilbert transform, thus it can be classified as a passive IDM. The outcome of the used Hilbert transform algorithm is an analytical complex signal:

$$y(t) = f(t) + j\hat{f}(t), \quad (23)$$

where  $f(t)$  is a real function and  $\hat{f}(t)$  is its Hilbert transform, which, in the time domain, is a convolution between the Hilbert transformer  $1/(\pi t)$  and the original signal  $f(t)$ :

$$\hat{f}(t) = f(t) * \frac{1}{\pi t} = \frac{1}{\pi} P \int_{-\infty}^{+\infty} \frac{f(\tau)}{t - \tau} d\tau \quad (24)$$

where  $P$  represents the Cauchy principal value. By means of some mathematical manipulations, it is easy to verify that a real function and its Hilbert transform are orthogonal. The polar representation of the analytical complex signal is:

$$y(t) = e(t) e^{j\varphi(t)} \quad (25)$$

where  $\varphi(t) = \tan^{-1}[\hat{f}(t)/f(t)]$  is the instantaneous phase, while  $e(t) = \sqrt{f^2(t) + \hat{f}^2(t)}$  is the instantaneous amplitude or rather the envelope of the original signal. In our case, it is the envelope of the PCC voltage  $e_A$ :

$$e(t) = \sqrt{e_A^2(t) + \hat{e}_A^2(t)} \quad (26)$$

The grid trip event determines a large spike in the monitored quantity (Equation (26)), which exceeds a suitable permitted range, thus allowing proper and quick detection of the grid fault. In fact, the proposed islanding detection method is carried out by monitoring the envelope of the original sampled voltage  $e_A$  (i.e., the line-to-line voltage) at PCC. In particular, a moving window of 20 ms (i.e., one grid cycle) with a time shift of 5 ms is used to evaluate the envelope, but only the center value in the window is considered to detect the possible grid outage with the aim of excluding the edge effects that could produce a false positive.

As a consequence, after a grid trip event, the maximum time requested to detect the islanding is equal to 12.5 ms (i.e., 10 ms due to half of the window length plus half the time shift), while in case the grid trip event results in synchronization with the grid period, the minimum time of 10 ms is required to detect the network failure.

Once this event is detected, the control section rapidly acts in order to disconnect the grid from the PV inverter by means of the proper circuit breaker interposed between the inverter and the utility

network (see also Figure 2). Moreover, the selection signal (i.e.,  $sel$  in Figure 2) provided by the islanding detection block is able to commutate the control in order to take into account the new system configuration.

In fact, in islanded mode, the control of the displacement angle  $\alpha$  is no longer needed, while the dynamics of DC-link voltage  $v_{out}$  are now useful in order to control the BESS, which acts to guarantee the energy continuity to the critical local load. As a consequence, an increase of the voltage  $v_{out}$  means that the load power request is greater than the PV generated one; the BESS should provide the needed amount of power to cover the load demand, while, when the power load request is lower than generated one, the BESS can accumulate the excess of power from the PVG.

### 3.3. Islanded Mode

During islanding operation, the system dynamic behavior consequently changes. In fact, the presence of the BESS must be considered in order to properly control the power flow (i.e.,  $i_{sto} \neq 0$  in Equation (1)). In such a case, by considering the state space averaged model of the step-up converter in Equation (1), the magnetizing current reference can be written as:

$$I_m^{ref} = \frac{1 + r_n}{1 - D} I_{out}^{ref} = \frac{1 + r_n}{1 - D} \frac{V_{in}^{ref}}{V_{out}^{ref}} (i_{pv} + i_{sto}) \quad (27)$$

where the reference storage current is obtained by the PI controller as reported in Figure 2. Then, the same reasoning as in Sub-Section 3.1 can be here repeated in order to obtain a suitable sliding mode control law. Moreover, in the relationship in Equation (2),  $i_j$  is zeroed due to activation of the breaker, while the dynamic behavior of DC-link voltages remains the same as described in Equation (3).

The control of the second power stage no longer takes into account the displacement angle  $\alpha$  because of grid tripping. Thus, the reference quantities (subscript index 2) for the load line-to-line voltages (i.e.,  $v_{pA}$ ,  $v_{pB}$ ) and also for their derivative (subscript index 1) of the two-phase system can be described by the vector:

$$\mathbf{x}_{rj} = [x_{rj1}, x_{rj2}]^T \quad (28)$$

where the two components of  $\mathbf{x}_{rj}$  for  $j = A, B$  are:

$$\begin{cases} x_{rA1} = -\sqrt{2} \omega V_p^{ref} \sin(\omega t + \vartheta) \\ x_{rA2} = \sqrt{2} V_p^{ref} \cos(\omega t + \vartheta) \\ x_{rB1} = -\sqrt{2} \omega V_p^{ref} \sin(\omega t + \vartheta + \pi/3) \\ x_{rB2} = \sqrt{2} V_p^{ref} \cos(\omega t + \vartheta + \pi/3) \end{cases} \quad (29)$$

Then, the sliding surface can be obtained as in Equation (21) by considering the properly modified circuit variables.

## 4. Numerical Results

A set of simulations is carried out on the grid-connected PV system (see Figure 2) in PLECS environment. The system under study is implemented by using the circuit parameters listed in Table 1.

**Table 1.** Used circuit parameters.

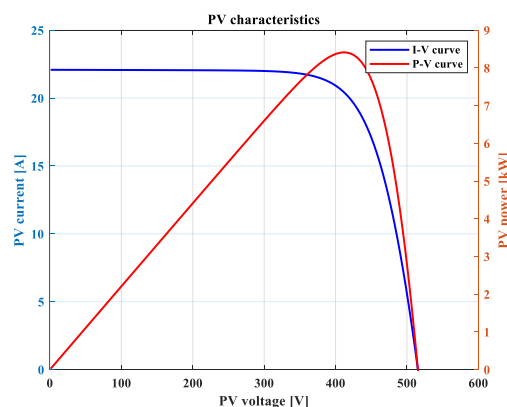
Parameters	Values
$E$ (V)	400
$C_{in}$ (mF)	10
$L$ (mH)	20
$R_1$ (m $\Omega$ )	27.14
$R_2$ (m $\Omega$ )	67.86
$L_f$ (mH)	10
$C_f$ (mF)	0.5
$R_t$ (m $\Omega$ )	0.267
$L_t$ (mH)	8.46

The PV array is described by a physical model based on the five parameters single diode model, where the unknown parameters are:  $I_{ph}$  (photo-generated current),  $I_0$  (reverse saturation current),  $R_s$  (parasitic series resistance),  $R_{sh}$  (parasitic shunt resistance), and  $a$  (diode ideality factor). The aim is the evaluation of these parameters at Standard Test Conditions (STC) and also under varying environmental conditions by using data-sheet information. As a consequence, the parameters of the PV model are estimated, and the used values are reported in Table 2, where  $V_t = a k T_{STC}/q$  is the thermal voltage,  $T_{STC}$  is the junction temperature at STC, and  $n_s$  is the number of cells.

**Table 2.** Estimated input parameters of a PV module.

Parameters	Values
$I_{ph}$ (A)	7.362
$I_0$ (A)	0.351
$a$	1.2
$V_t$ (V)	0.025
$R_s$ ( $\Omega$ )	0.204
$R_{sh}$ ( $\Omega$ )	1168
$n_s$	60

The considered PVG consists of a PV array with  $N_s = 17$  series connected panels (i.e., PV string) and  $N_p = 3$  parallel connected strings to reach the desired power level. Figure 4 shows the current–voltage (I–V) and the power–voltage (P–V) characteristics of the considered PV array in Standard Conditions. The corresponding MPP values are  $V_{MPP} = 412$  V,  $I_{MPP} = 20.4$  A,  $P_{MPP} = 8.41$  kW. Moreover, the used control parameters are summarized in Table 3.

**Figure 4.** Current–voltage (I–V) and power–voltage (P–V) curves at Standard Test Conditions (STC).

**Table 3.** Control parameters.

Parameters	Values
$T_{MPPT}$ (ms)	100
$\Delta V_{MPPT}$ (V)	1
$v_{MPPT}^{ref}$ (V)	414.2
$\beta_1$	0.5
$\beta_2$	-1
$\Delta$	1
$\sigma_1$	0.001
$\sigma_2$	1
$\sigma_3$	0.06
$\sigma_4$	0.06
$\Delta'$	4

Regarding the sizing of the battery pack, the most relevant parameter to take into account is the battery capacity, which is assumed constant, even in cases of different discharging current rates, in order to simplify the model. The other main parameters are the stored energy and the State of Charge (SOC). The latter is reported in the following Equation:

$$SOC(t) = SOC(t_0) - \frac{1}{Q_0} \int_{t_0}^t i_b \, d\tau \quad (30)$$

where  $Q_0$  is the total charge storable in the battery, while  $i_b$  is the discharging current.

A simplified circuital model is implemented to describe the behavior of the BESS. The equivalent circuit is the series of a voltage source providing the open-circuit voltage  $V_{oc}$  and a lumped resistor  $R_{int}$ , modeling internal resistance of batteries. The open-circuit voltage is dynamically obtained as function of the SOC by the following non-linear relationship:

$$V_{oc} = E_0 + \frac{RT}{F} \log\left(\frac{SOC}{1-SOC}\right) \quad (31)$$

where  $E_0$  is the standard potential of the battery,  $R$  is the ideal gas constant,  $T$  is the absolute temperature, and  $F$  is the Faraday constant. The size of the battery results from the need to support the PV power generation in order to meet the load demand. As a consequence, a storage unit should be able to provide the total rated load power (i.e., 4 kW) for an hour, corresponding to a battery energy of 4 kWh. This choice allows one to overcome a grid trip and also to mitigate the inherent variability of PV production while ensuring a continuous power supply to critical load. Hence, the used BESS presents a capacity of 20 Ah with a rated voltage of about 200 V and total internal resistance of 30 m $\Omega$ .

The load is considered pure resistive, and the chosen resistance of each load is equal to the *rms* line-to-line grid voltage divided by the corresponding power  $R_A = R_B = E^2/P_{load} = 80 \, \Omega$  (see Figure 2). Moreover, an additional load in parallel with the grid is considered to take into account other loads on the grid network, which may continue to be supplied by the inverter after the grid trip and before the grid disconnection. These additional loads are assumed to be an order of magnitude greater than the local load.

#### 4.1. Normal Operation and Islanding Detection

In this work, we paid particular attention to both islanding detection and BESS control in order to guarantee fault tolerant operation of the inverter. The load demand is globally set at 4 kW (i.e., 2 kW for each load), while the PVG is considered to be operated at STC, thus leading to a PV power production of about 8.4 kW. In such a case, the power difference between PV available power and load demand is transferred to the grid with unity power factor due to the proper control of the displacement angle  $\alpha$ , which assumes a positive value. As a consequence, the main issue to be addressed is represented by

the islanding detection and the consequent disconnection from the utility network within the time constraint fixed by standard rules [27], which is typically 2 s.

Figure 5 shows the behavior of the PV voltage, which tracks stably the desired MPP in steady-state, thus leading to an MPPT efficiency of 99%. Furthermore, the control strategy allows one to obtain the desired voltage level at the inverter input (see Figure 6a) by means of well-balanced voltages  $v_{c1}$ ,  $v_{c2}$  at the DC-link (see Figure 6b,c).

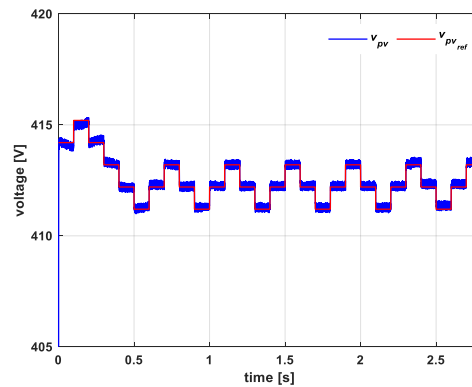


**Figure 5.** PV voltage (blue line) vs. maximum power point tracking (MPPT) reference voltage (red line).

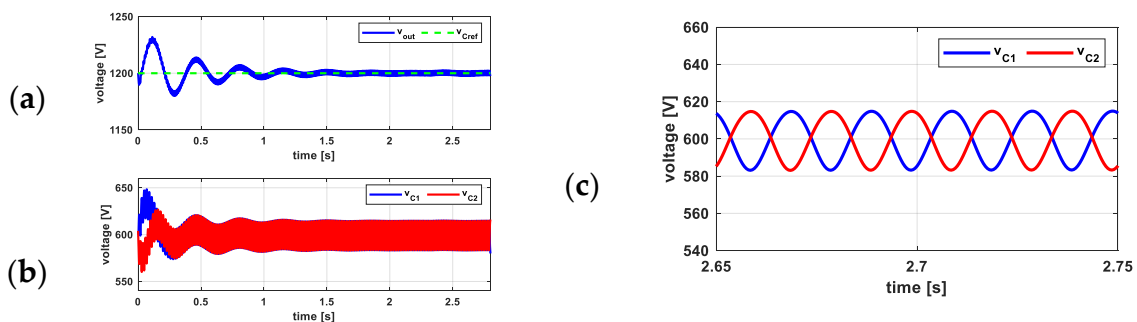


**Figure 6.** Time behavior of DC-link voltage: (a) total DC-link voltage; (b) separate DC-link voltage at each capacitor; (c) zoom view of separate DC-link voltage at each capacitor.

The time behavior of the displacement angle  $\alpha$  is drawn in Figure 7; as expected, it assumes a positive value, which means that the excess power (i.e., the difference between PV power generation and load power request) is transferred to the grid. The voltage and the current behavior of the latter are shown in Figure 8. The grid currents results are sinusoidal and in phase with the grid voltages, thus leading to an almost unity power factor.

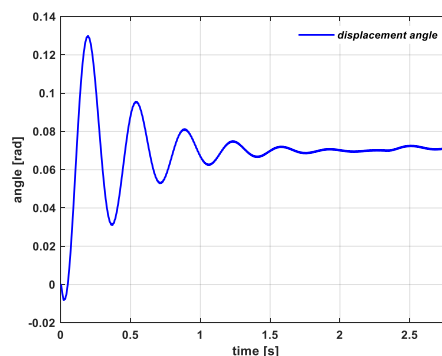


**Figure 7.** Time behavior of displacement angle  $\alpha$ .

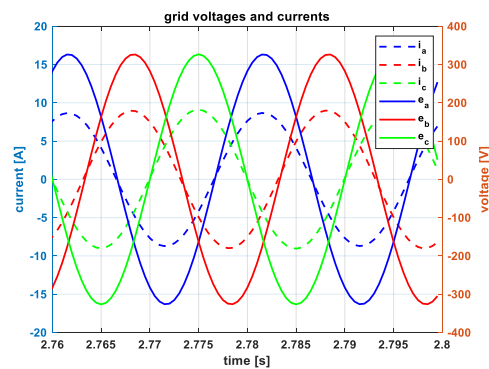


Figure 8. Steady-state behavior of grid currents and voltages.

The steady-state behavior of the load current is in Figure 9a, while Figure 9b shows the power at steady-state. It can be noted that PV excess power with reference to the load power demand is transferred to the grid.

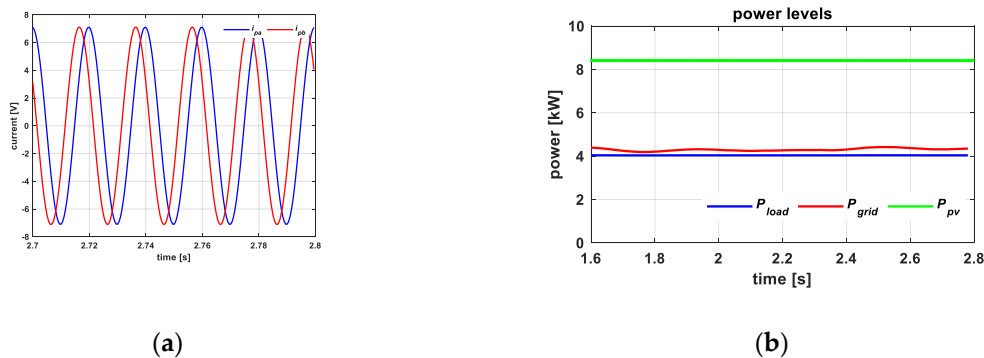


Figure 9. Steady-state behavior of load currents (a) and of power (b): load power (blue line), PV power (green line), and grid power (red line).

Figure 10 shows the results of the proposed ID method. The circles correspond to the envelope value in the middle of the chosen moving window, which has a time duration of 20 ms, as highlighted in the figure and discussed in Sub-Section 3.2. The arrow lines identify the sliding windows, while the colors are the same of the corresponding envelope detected value. The detection happens when the PCC voltage envelope falls outside a suitable safety range, whose typical upper and lower limits are  $+10\%/ -15\%$  of the rated value. In our case, in a conservative way, we considered a range of  $\pm 10\%$  of the rated value equal to  $\sqrt{2} E$  (i.e., the voltage interval (509–622 V) defined by the blue and red lines in Figure 10).

The grid fault event occurs at  $t = 3$  s (i.e., after 200 ms, it reached steady-state condition). The first value of the envelope that lies outside the safety range is the green circle, which represents the center of the window identified with the green arrow line. Nevertheless, as previously discussed, the grid trip event can be detected only at the end of the window or rather, in such a case, 10 ms after the event itself.

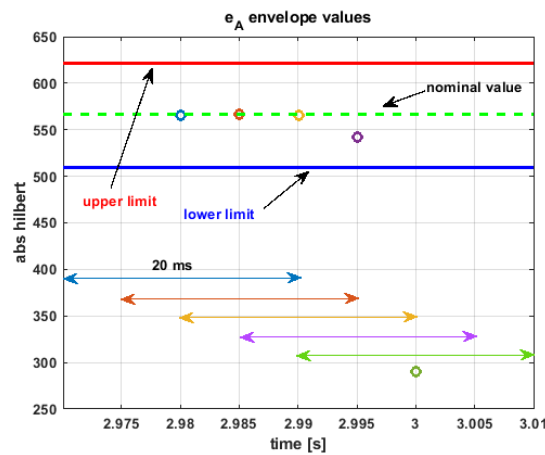


Figure 10. Point of common coupling (PCC) voltage envelope middle values (circles).

#### 4.2. Islanded Mode

Once the grid trip is detected, the control strategy must properly act to prevent supplying the network by disconnecting the inverter, which must continue to feed the critical local load.

The PV and the DC-link voltage behaviors in islanding mode are depicted in Figure 11. The grid trip event occurs at 3 s, while its detection is at 3.01 s, which is the time instant when the inverter is disconnected from the grid and the new control action starts.

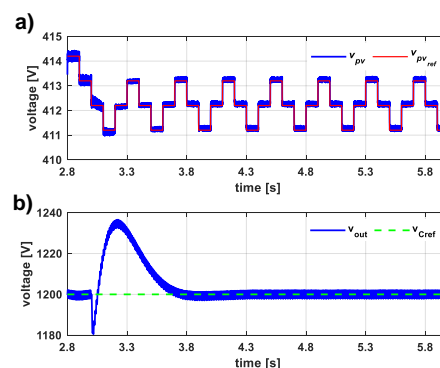


Figure 11. PV and the DC-link voltage behaviors: (a) PV voltage (blue line) and maximum power point (MPP) voltage reference (red line); (b) DC-link voltage (blue line) and corresponding reference voltage.

The MPP tracking is lost during only one MPPT cycle after the grid fault, while the DC-link voltage diverges from its reference with a maximum overshoot of 0.3% of the reference and recovers the desired behavior in a time interval lower than 1 s.

The time behavior of the BESS is drawn in Figure 12; initially (i.e., during normal operation), the battery is in idle mode (battery voltage is equal to the rated value of 200 V, battery current is zero, and the SOC is equal to its initial value of 50%). Once the grid trip is detected, the control section activates the battery, which can absorb (i.e., BESS charging) the PV power not used by the load; the system operates in island mode without undesired curtailment of PV production. Otherwise, the battery can provide the difference of the PV power with respect to the load demand, ensuring a continuous power supply to the critical load and enhancing system reliability and flexibility.

Finally, in Figure 13, the steady-state load current and the system power behavior are depicted.

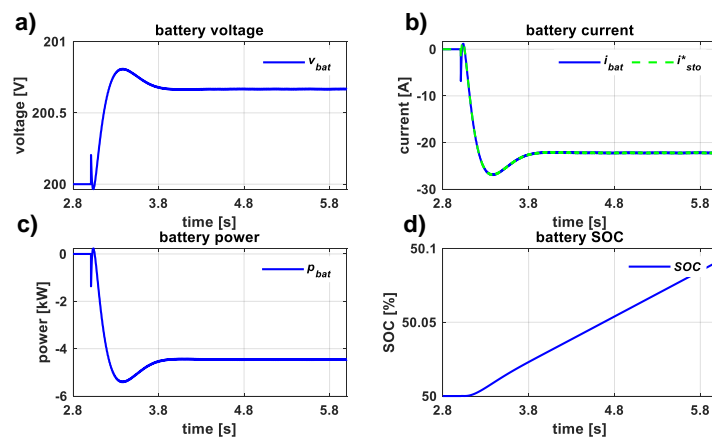


Figure 12. BESS time behavior: (a) voltage; (b) current; (c) power; (d) State of Charge (SOC).

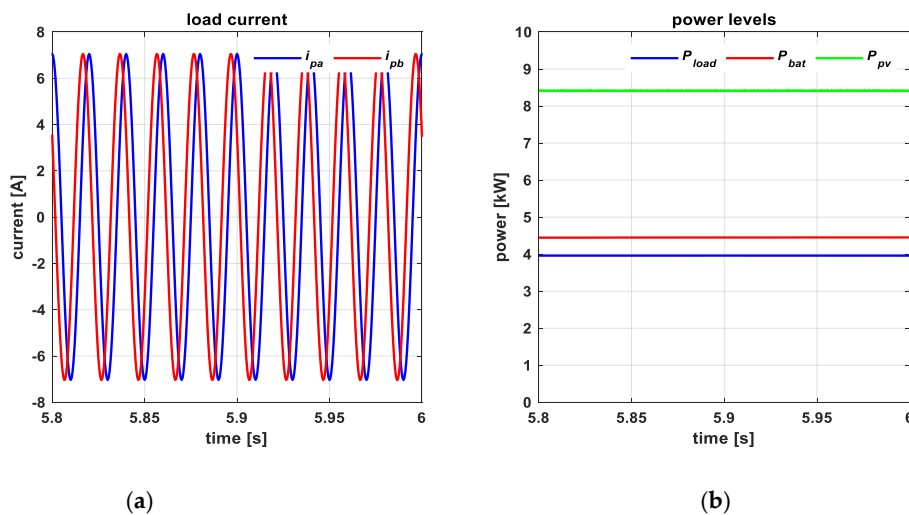


Figure 13. Steady-state behavior of load currents: (a) and of power (b); load power (blue line), PV power (green line), and battery power (red line).

It can be noted (see Figure 13a) that the load current is the same of Figure 9a, or rather no detrimental effect on the load arises from the grid trip event. In addition, Figure 13b shows how the PV power (i.e., about 8.4 kW) is higher than load demand (i.e., 4 kW). The excess power, which usually would be lost, is provided to the battery, leading to a flat power transfer to the load.

## 5. Conclusions

This paper is mainly focused on the control of a fault tolerant and reconfigurable grid-connected photovoltaic inverter. The main issue addressed is the possibility to continuously supply critical local load in case of a grid trip event and regardless of the inherent fluctuating nature of the energy generated by PV sources. As a consequence, a suitable islanding detection method is presented and implemented by monitoring the PCC voltage envelope evaluated by means of the Hilbert transform.

A complete set of numerical simulations proved the good performance in normal operation as well as the capability to detect a grid fault event in few milliseconds, thus fully accomplishing the standard requirements. In particular, the minimum time requested to detect the grid outage is equal to 12.5 ms, which can be further reduced to 10 ms in case the grid trip event results in synchronization with the grid period. The proposed IDM appears to be very fast, and it can be compared in terms of speed with respect to different techniques proposed in recent research works, thus showing its benefit in being independent of the specific application.

Moreover, in islanded mode, the system remains fully functional due to a suitable modification of the control strategy, which exploits the integrated *BESS* to continuously provide a flat profile of the load power. Finally, adequate system performance in terms of power quality, power factor, and MPPT efficiency also proves the effectiveness of the proposed control approach.

**Author Contributions:** Conceptualization, D.L., M.C., and P.G.; methodology, D.L., M.C., and P.G.; software, M.C., P.G., and A.D.; validation, M.C., P.G., and A.D.; formal analysis, D.L. and M.C.; investigation, M.C., P.G., and A.D.; resources, D.L., S.D., and A.D.P.; data curation, M.C.; writing—original draft preparation, M.C., P.G., and A.D.P.; writing—review and editing, A.D.P., D.L., S.D., and A.D.; visualization, M.C., P.G., and A.D.; supervision, A.D.P., D.L., and S.D. All authors have read and agreed to the published version of the manuscript.

**Funding:** This research received no external funding.

**Conflicts of Interest:** The authors declare no conflict of interest.

## Nomenclature

$C_1; C_2$	DC-link capacitors
$C_{bat}$	input capacitor of bidirectional DC-DC converter
$C_{in}$	input capacitor
$E$	<i>rms</i> line-to-line grid voltage
$e_A; e_B$	linetoline voltages
$i_{bat}$	battery current
$i_{pv}$	PV current
$i_{sto}$	storage current
$i_{invA}; i_{invB}$	inverter output currents
$i_{pA}; i_{pB}$	load currents
$k$	coupling coefficient
$L$	total inductance of coupled inductors
$L_0$	inductance of a single winding
$L_1; L_2$	primary and a secondary inductor
$L_f; C_f$	inverter output filter
$N_1; N_2$	turn number of the primary and secondary inductor
$R_1; R_2$	resistors account for inductors copper losses
$r_n$	winding ratio of the magnetically coupled inductors
$R_A; R_B$	load resistors
$R_t; L_t$	equivalent parameters of line three-phase transformer
$S$	circuit breaker activation signal
$sel$	demux selection signal
$u$	driving signal of coupled inductors DC-DC converter
$u_j$	driving signal of inverter stage
$v_{bat}$	battery voltage
$v_{C1}, v_{C2}$	Dclink voltages
$v_{in}$	PV voltage
$v_{invA}; v_{invB}$	inverter output voltages
$v_{pA}; v_{pB}$	linetoline load voltages
$v_{out}$	total Dclink voltage
$v_{MPPT}^{ref}$	MPPT voltage reference
$\alpha$	angle between load voltages and network voltages
$\beta_1; \beta_2$	coefficients of coupled inductors DC-DC converter sliding surface
$x_1; x_2$	statevariables error of coupled inductors DC-DC converter sliding control
$\mathbf{x}_{ej}$	vector of the statevariables error of inverter sliding control
$\Delta$	half the amplitude of the hysteresis band in the sliding surface of coupled inductors DC-DC converter
$\Delta'$	half the amplitude of the hysteresis band in the sliding surface of inverter
$\sigma_1, \sigma_2, \sigma_3, \sigma_4$	coefficients of inverter sliding surface

BESS	battery energy storage system
BMS	battery management system
DER	distributed energy resources
EPS	electric power systems
ID	islanding detection
IDM	islanding detection method
MPP	maximum power point
MPPT	maximum power point tracking
PCC	point of common coupling
P&O	perturb and observe
PV	photovoltaic
PVG	photovoltaic generator
RES	renewable energy sources
SOC	state of charge

## References

1. Kouro, S.; Leon, J.I.; Vinnikov, D.; Franquelo, L.G. Grid-Connected Photovoltaic Systems: An Overview of Recent Research and Emerging PV Converter Technology. *IEEE Ind. Electron. Mag.* **2015**, *9*, 47–61. [\[CrossRef\]](#)
2. Romero-Cadaval, E.; Spagnuolo, G.; Franquelo, L.G.; Ramos-Paja, C.A.; Suntio, T.; Xiao, W.M. Grid-Connected Photovoltaic Generation Plants: Components and Operation. *IEEE Ind. Electron. Mag.* **2013**, *7*, 6–20. [\[CrossRef\]](#)
3. Romero-Cadaval, E.; Francois, B.; Malinowski, M.; Zhong, Q. Grid-Connected Photovoltaic Plants: An Alternative Energy Source, Replacing Conventional Sources. *IEEE Ind. Electron. Mag.* **2015**, *9*, 18–32. [\[CrossRef\]](#)
4. European Technology & Innovation Platform. Available online: <https://etip-pv.eu/> (accessed on 6 March 2020).
5. Liserre, M.; Sauter, T.; Hung, J.Y. Future Energy Systems: Integrating Renewable Energy Sources into the Smart Power Grid through Industrial Electronics. *IEEE Ind. Electron. Mag.* **2010**, *4*, 18–37. [\[CrossRef\]](#)
6. Petrone, G.; Spagnuolo, G.; Teodorescu, R.; Veerachary, M.; Vitelli, M. Reliability Issues in Photovoltaic Power Processing Systems. *IEEE Trans. Ind. Electron.* **2008**, *55*, 2569–2580. [\[CrossRef\]](#)
7. Zeineldin, H.H.; El-Saadany, E.F.; Salama, M.M.A. Impact of DG interface control on islanding detection and nondetection zones. *IEEE Trans. Power Deliv.* **2006**, *21*, 1515–1523. [\[CrossRef\]](#)
8. Yu, B.; Matsui, M.; Yu, G. A review of current anti-islanding methods for photovoltaic power system. *Sol. Energy* **2010**, *84*, 745–754. [\[CrossRef\]](#)
9. Teodorescu, R.; Liserre, M.; Rodríguez, P. *Grid Converters for Photovoltaic and Wind Power Systems*; John Wiley & Sons Ltd.: Hoboken, NJ, USA, 2011.
10. Kim, M.-S.; Haider, R.; Cho, G.-J.; Kim, C.-H.; Won, C.-Y.; Chai, J.-S. Comprehensive Review of Islanding Detection Methods for Distributed Generation Systems. *Energies* **2019**, *12*, 837. [\[CrossRef\]](#)
11. Ku Ahmad, K.N.E.; Selvaraj, J.; Rahim, N.A. A review of the islanding detection methods in grid-connected PV inverters. *Renew. Sustain. Energy Rev.* **2013**, *21*, 756–766. [\[CrossRef\]](#)
12. Reddy, V.R.; Sreeraj, E.S. A Feedback-Based Passive Islanding Detection Technique for One-Cycle-Controlled Single-Phase Inverter Used in Photovoltaic Systems. *IEEE Trans. Ind. Electron.* **2019**, *67*, 6541–6549. [\[CrossRef\]](#)
13. Rostami, A.; Jalilian, A.; Zabihi, S.; Olamaei, J.; Pouresmaeil, E. Islanding Detection of Distributed Generation Based on Parallel Inductive Impedance Switching. *IEEE Syst. J.* **2020**, *14*, 813–823. [\[CrossRef\]](#)
14. Bakhshi-Jafarabadi, R.; Sadeh, J.; Popov, M. Maximum Power Point Tracking Injection Method for Islanding Detection of Grid-Connected Photovoltaic Systems in Microgrid. *IEEE Trans. Power Deliv.* **2020**. [\[CrossRef\]](#)
15. Babak, S.; Mohamad Esmaeil, H.-G.; Iman, S. Comprehensive investigation of the voltage relay for anti-islanding protection of synchronous distributed generation. *Int. Trans. Elect. Energy Syst.* **2017**, *27*, 1–16.
16. Abyaz, A.; Panahi, H.; Zamani, R.; Haes Alhelou, H.; Siano, P.; Shafie-khah, M.; Parente, M. An Effective Passive Islanding Detection Algorithm for Distributed Generations. *Energies* **2019**, *12*, 3160. [\[CrossRef\]](#)
17. Haider, R.; Kim, C.H.; Ghanbari, T.; Bukhari, S.B.A.; Zaman, M.S.; Baloch, S.; Oh, Y.S. Passive islanding detection scheme based on autocorrelation function of modal current envelope for photovoltaic units. *IET Gener. Transm. Distrib.* **2018**, *12*, 726–736. [\[CrossRef\]](#)

18. Sirico, C.; Teodorescu, R.; Séra, D.; Coppola, M.; Guerriero, P.; Iannuzzi, D.; Dannier, A. PV Module-Level CHB Inverter with Integrated Battery Energy Storage System. *Energies* **2019**, *12*, 4601. [[CrossRef](#)]
19. Lauria, D.; Coppola, M. Design and control of an advanced PV inverter. *Solar Energy* **2014**, *110*, 533–542. [[CrossRef](#)]
20. Coppola, M.; Lauria, D.; Napoli, E. On the design and the efficiency of coupled step-up dc-dc converters. In Proceedings of the IEEE International Conference on Electrical Systems for Aircraft, Railway and Ship Propulsion (ESARS), Bologna, Italy, 19–21 October 2010.
21. Coppola, M.; Lauria, D.; Napoli, E. Optimal design and control of coupled-inductors step-up dc-dc converter. In Proceedings of the 2011 IEEE International Conference on Clean Electrical Power (ICCEP), Ischia, Italy, 14–16 June 2011; pp. 81–88.
22. Guerriero, P.; Coppola, M.; Cennamo, P.; Daliento, S.; Lauria, D. A single panel PV microinverter based on coupled inductor DC-DC. In Proceedings of the 2017 IEEE International Conference on Environment and Electrical Engineering and 2017 IEEE Industrial and Commercial Power Systems Europe (EEEIC/I & CPS Europe), Milan, Italy, 6–9 June 2017; pp. 1–5.
23. IEEE. *1547–2018-IEEE Standard for Interconnection and Interoperability of Distributed Energy Resources with Associated Electric Power Systems Interfaces*; IEEE: Piscataway, NJ, USA, 2018.
24. Dwari, S.; Jayawant, S.; Beechner, T.; Miller, S.K.; Mathew, A.; Min, C.; Riehl, J.; Sun, J. Dynamics Characterization of Coupled-Inductor Boost DC-DC Converters. In Proceedings of the 2006 IEEE Workshops on Computers in Power Electronics, Troy, NY, USA, 16–19 July 2006.
25. Skvarenina, T.L. *The Power Electronics Handbook*; CRC Press: Boca Raton, FL, USA, 2002; Chapter 8.
26. Mattavelli, P.; Rossetto, L.; Spiazzi, G. Small-signal analysis of DC-DC converters with sliding mode control. *IEEE Trans. Power Electron.* **1997**, *12*, 96–102. [[CrossRef](#)]
27. IEEE. *1547.1–2005-IEEE Standard Conformance Test Procedures for Equipment Interconnecting Distributed Resources with Electric Power Systems, IEEE Std.*; IEEE: Piscataway, NJ, USA, 2005; ISBN 0-7381-4736-2 SH95346.



© 2020 by the authors. Licensee MDPI, Basel, Switzerland. This article is an open access article distributed under the terms and conditions of the Creative Commons Attribution (CC BY) license (<http://creativecommons.org/licenses/by/4.0/>).